# NATURAL CONVECTION IN A CLOSED CAVITY UNDER STOCHASTIC, NON-BOUSSINESQ CONDITIONS*

OLIVIER LE MAÎTRE[†], M.T. REAGAN[‡], B. DEBUSSCHERE[§], H.N. NAJM[¶], R.G. GHANEM[‖], AND O.M. KNIO[**]

**Abstract.** A stochastic projection method (SPM) is developed for quantitative propagation of uncertainty in compressible zero-Mach-number flows. The formulation is based on a spectral representation of uncertainty using the Polynomial Chaos (PC) system, and on a Galerkin approach to determine the PC coefficients. Governing equations for the stochastic modes are solved using a mass-conservative projection method. The formulation incorporates a specially tailored stochastic inverse procedure for exactly satisfying the mass-conservation divergence constraints. A brief validation of the zero-Mach-number solver is first performed, based on simulations of natural convection in a closed cavity. The SPM is then applied to analyze the steady-state behavior of the heat transfer and of the velocity and temperature fields under stochastic non-Boussinesq conditions.

**Key words.** Stochastic, Natural Convection, Navier-Stokes, Polynomial Chaos, Karhunen-Loève, Uncertainty

## 1. Introduction.

Low-Mach-number flows arise in a wide class of important applications, including thermal transport and management as well as burners and combustors. In many cases, these applications rely on complex physical models that involve inexact knowledge of system parameters or operating conditions. This effort aims at the development of uncertainty propagation and quantification methods for zero-Mach-number compressible flows.

In a previous effort [16], a stochastic projection method (SPM) for incompressible flows was developed, based on spectral representation of uncertain parameters in terms of the Polynomial Chaos (PC) system [27, 1, 3, 22, 23, 5, 4, 11]. In subsequent work [15], the physical model was extended to Boussinesq flow, and the stochastic formulation was generalized in order to accommodate both random parameters as well as uncertain model data corresponding to a random process. The latter is modeled in [15] as a Gaussian process, which is efficiently represented in terms of the Karhunen-Loève expansion [20].

The objective of the present effort is to generalize the stochastic Boussinesq

[†]Centre d'Etudes de Mécanique d'Ile de France, Université d'Evry Val d'Essone, 40, rue du Pelvoux, 91020 Evry cedex, France (olm@iup.univ-evry.fr).

[‡]Combustion Research Facility, Sandia National Laboratories, Livermore, CA 94550 (mtreaga@ca.sandia.gov).

[§]Combustion Research Facility, Sandia National Laboratories, Livermore, CA 94550 (bjdebus@ca.sandia.gov).

[¶]Combustion Research Facility, Sandia National Laboratories, Livermore, CA 94550 (hnnajm@ca.sandia.gov).

[‖]Department of Civil Engineering, The Johns Hopkins University Baltimore, MD 21218 (ghanem@jhu.edu).

[**]Department of Mechanical Engineering, The Johns Hopkins University Baltimore, MD 21218 (knio@jhu.edu).

scheme in [15] to a stochastic zero-Mach-number solver. To illustrate the development, we focus on the same physical setup introduced in [15], namely on natural convection in a closed cavity. Specifically, the problem consists of a square or rectangular cavity with adiabatic horizontal boundaries and differentially but uniformly heated vertical walls (e.g. [6, 2, 18, 17, 19]).

However, unlike the Boussinesq analysis in [15], the assumption of weak temperature difference is no longer invoked. In order to adequately address the present setting, in section 2 a zero-Mach-number physical model [21, 19, 25, 14] is introduced. A stochastic variant of the deterministic problem, first introduced in [15], is also used. As summarized in section 3, it consists of treating the cold wall as having a uniform temperature and imposing a stochastic temperature distribution on the hot vertical boundary. The zero-Mach-number stochastic solution scheme is then constructed. As outlined in section 4, the construction combines a PC representation of random variables with a mass-conservative [25] projection scheme. In section 5, a brief validation study of the stochastic solver is performed, based on comparing the resulting predictions with available results from the literature. The scheme is then applied in section 6 to analyze the behavior of steady-state heat transfer and of the velocity and temperature fields within the cavity under stochastic, non-Boussinesq conditions. Major conclusions are summarized in section 7.

**2. Deterministic System.** As mentioned in the introduction, the physical setup used is identical to the one in [15]. Specifically, we consider a square 2D cavity of side $\tilde{L}$, filled with a variable-property Newtonian fluid of density $\tilde{\rho}$, molecular viscosity $\tilde{\mu}$, thermal conductivity $\tilde{\kappa}$, and temperature $\tilde{T}$. A Cartesian $(\tilde{x}, \tilde{y})$ coordinate system is selected with $\tilde{y}$ pointing vertical and $\tilde{x}$ horizontal. The two horizontal walls of the cavity are assumed adiabatic, while the left and right vertical walls are maintained at uniform temperature, $\tilde{T}_h$ and $\tilde{T}_c$ respectively. The mean temperature $\tilde{T}_0$ is defined as $\tilde{T}_0 \equiv (\tilde{T}_h + \tilde{T}_c)/2$. Tildes are used to denote dimensional quantities and the subscript 0 is used to denote reference quantities. Using the mean temperature, and the temperature difference between the hot and cold walls, $\Delta\tilde{T} \equiv \tilde{T}_h - \tilde{T}_c$, we introduce the Boussinesq ratio $\epsilon \equiv \Delta\tilde{T}/2\tilde{T}_0$.

**2.1. Zero-Mach-Number Model.** A zero-Mach-number [21, 19, 25, 14] flow model is used to describe the dynamics of the heated cavity. In this limit, the action of acoustic waves is ignored and the pressure is decomposed into a hydrodynamic component $\Pi(\boldsymbol{x}, t)$ and a spatially uniform thermodynamic component $\overline{P}(t)$. Following these assumptions, we will thus be concerned with the numerical solutions of the following set of normalized governing equations:

$$(2.1) \qquad \frac{\partial \rho}{\partial t} = -\boldsymbol{\nabla} \cdot \rho\boldsymbol{u}$$

$$(2.2) \qquad \frac{\partial u}{\partial t} = -\frac{\partial(\rho u^2)}{\partial x} - \frac{\partial(\rho uv)}{\partial y} - \frac{\partial\Pi}{\partial x} + \frac{1}{\sqrt{\mathrm{Ra}}}\Phi_x$$

$$(2.3) \qquad \frac{\partial v}{\partial t} = -\frac{\partial(\rho uv)}{\partial x} - \frac{\partial(\rho v^2)}{\partial y} - \frac{\partial\Pi}{\partial y} + \frac{1}{\sqrt{\mathrm{Ra}}}\Phi_y - \frac{1}{\mathrm{Pr}}\frac{\rho - 1}{2\epsilon}$$

$$(2.4) \qquad \frac{\partial T}{\partial t} = -\boldsymbol{u} \cdot \boldsymbol{\nabla} T + \frac{1}{\rho\mathrm{Pr}\sqrt{\mathrm{Ra}}}\boldsymbol{\nabla} \cdot (\kappa\boldsymbol{\nabla} T) + \frac{\gamma - 1}{\rho\gamma}\frac{d\overline{P}}{dt}$$

$$(2.5) \qquad \overline{P} = \rho T$$

where $\rho$ is the density, $\boldsymbol{u} = (u, v)$ is the velocity field, $\Pi$ is the hydrodynamic pressure, $\mathrm{Ra} = \tilde{g}\beta\Delta\tilde{T}\tilde{L}^3/\tilde{\nu}_0\tilde{\alpha}_0$ is the Rayleigh number, $\beta$ is thermal expansion coefficient, $\tilde{g}$ is

the gravitational acceleration, $\Phi_x$ and $\Phi_y$ are the viscous stress terms in the $x$ and $y$ directions, respectively, $\mathrm{Pr} = \tilde{\nu}_0/\tilde{\alpha}_0$ is the Prandtl number (here equal to 0.7), $\kappa \equiv \tilde{\kappa}/\tilde{\kappa}_0$ is the normalized thermal conductivity, $\gamma$ is the specific heat ratio, and $\overline{P}(t)$ is the thermodynamic pressure [19]. Variables are normalized with respect to the appropriate combination of the reference temperature $\tilde{T}_0$, density $\tilde{\rho}_0$, length $\tilde{L}$, and velocity $\tilde{V}_0 \equiv \tilde{\nu}_0 \sqrt{\mathrm{Ra}}/\tilde{L}$.

The viscous stress terms are given by the divergence of the viscous stress tensor,

$$(2.6) \qquad \tau = \frac{\mu}{2} \left[ (\nabla \times \boldsymbol{u}) + (\nabla \times \boldsymbol{u})^T \right]$$

where $\mu \equiv \tilde{\mu}/\tilde{\mu}_0$ is the normalized viscosity. In the computations, the viscosity and thermal conductivity are assumed to be constant, or to depend on temperature according to the Sutherland law [19]:

$$(2.7) \qquad \kappa(T) = T^{3/2} \frac{1 + S_\kappa}{T + S_\kappa} \quad , \quad \mu(T) = T^{3/2} \frac{1 + S_\mu}{T + S_\mu}$$

where $S_\kappa = 0.648$ and $S_\mu = 0.368$. For brevity, most of the results presented below correspond to the constant property case.

The above system of equations is supplemented with no-slip boundary conditions on velocity, while adiabatic conditions ($\partial T/\partial y = 0$) are used on horizontal walls. For the left and right vertical boundaries, Dirichlet conditions on temperature are used, respectively $T = 1 + \epsilon$ and $T = 1 - \epsilon$. Initially, the fluid in the cavity is assumed to be in a state of rest, with uniform temperature ($T = 1$) and pressure ($P = 1$). The unsteady system of equations is integrated in time till steady conditions are reached.

**2.2. Boussinesq Limit.** In the Boussinesq limit $\epsilon \to 0$, substantial simplification of the above system can be implemented. Specifically, variation of the thermodynamic pressure and density can be essentially ignored, and the velocity field can be treated as divergence free [19]. In particular, the latter simplification enables the development of an incompressible flow solver, whose deterministic and stochastic forms are extensively discussed in [16, 15]. In the following section, we shall focus on extension of the stochastic Boussinesq solver [15] to zero-Mach-number flows under non-Boussinesq conditions.

**3. Stochastic Formulation.** As in [15], we consider the effect of "random" fluctuations on the cold wall. The normalized mean wall temperature at $x = 1$ is expressed as:

$$(3.1) \qquad T_1(y) \equiv T(x = 1, y) = T_c + T'(y) = 1 - \epsilon + T'(y)$$

Using angle-brackets to denote expectations, we have $< T_1 > = T_c = 1 - \epsilon$, i.e. $T'$ has vanishing expectation and the mean temperature along the cold wall is independent of $y$ and corresponds to $T_c$.

The random component is assumed to be given by a Gaussian process which is characterized by its normalized variance $\sigma_T^2$, and an auto-correlation function, $\mathcal{K}$, given by:

$$(3.2) \qquad \mathcal{K}(y_1, y_2) \equiv < T'(y_1) T'(y_2) > = \epsilon^2 \sigma_T^2 \exp\left[ -|y_1 - y_2|/L_c \right].$$

where $L_c$ is the normalized correlation length. $\mathcal{K}$ can be expanded in terms of its eigenvalues, $\lambda_i$, and eigenfunctions, $f_i(y)$, using [11, 10, 9]:

$$(3.3) \qquad \mathcal{K}(y_1, y_2) = \epsilon^2 \sum_{i=0}^{\infty} \lambda_i f_i(y_1) f_i(y_2).$$

and $T'$ can be accordingly expressed in the Karhunen-Loève (KL) expansion as [20]:

$$(3.4) \qquad T'(y) = \epsilon \sum_{i=0}^{\infty} \sqrt{\lambda_i} f_i(y) \xi_i.$$

where the $\xi_i$'s are uncorrelated Gaussian variables having vanishing expectation and unit variance.

As discussed in [11, 15], an analytical expression for the kernel in Eq. (3.2) is available:

$$(3.5) \qquad f_n(y) = \begin{cases} \dfrac{\cos[\omega_n(y - 1/2)]}{\sqrt{\dfrac{1}{2} + \dfrac{\sin(\omega_n)}{2\omega_n}}} & \text{if } n \text{ is even} \\[2em] \dfrac{\sin[\omega_n(y - 1/2)]}{\sqrt{\dfrac{1}{2} - \dfrac{\sin(\omega_n)}{2\omega_n}}} & \text{if } n \text{ is odd} \end{cases}$$

where

$$(3.6) \qquad \lambda_n = \sigma_T^2 \frac{2L_c}{1 + (\omega_n L_c)^2},$$

and $\omega_n$ are the positive (ordered) roots of the characteristic equation:

$$(3.7) \qquad [1 - L_c \omega \tan(\omega/2)] \, [L_c \omega + \tan(\omega/2)] = 0.$$

Since the first positive root of Eq. (3.7) is $\omega_0 = 0$, corresponding to $f_0 = 0$, Eq. (3.4) may be rewritten as:

$$(3.8) \qquad T'(y) = \epsilon \sum_{i=1}^{\infty} \xi_i \sqrt{\lambda_i} f_i(y).$$

In numerical tests, the KL expansion is truncated, and the temperature fluctuation is approximated as:

$$(3.9) \qquad T' = \epsilon \sum_{i=1}^{N_{KL}} \xi_i \sqrt{\lambda_i} f_i(y),$$

where $N_{KL}$ is the number of modes retained in the expansion. The errors associated with this truncation have been extensively analyzed in [15]. In the simulations below, we take advantage of the results of this prior analysis for the selection of the truncation parameter.

**4. Solution Scheme.** The solution scheme introduced below is a generalized form of the scheme developed in [16, 15]. Briefly, the same spectral stochastic representation of solution is adopted, based on the PC representation of field variables. This spectral representation is then inserted into the governing equations and a weighted residual approach is used to derive governing equations for the mode coefficients in the PC expansion. One fundamental difference between the present situation and that tackled in [15] arises due to the fact that higher order non-linearities arise in

the present set of governing equations whereas only second-order non-linearities are present in Boussinesq flow. Additional means are required to estimate the moments corresponding to these higher order non-linearities. An additional, more delicate, complication is that these higher order non-linearities appear in stochastic divergence constraints. As shown below, this necessitates the introduction of a specially tailored procedure in order to ensure that the corresponding solvability constraints are exactly satisfied.

**4.1. Spectral Stochastic Representation.** The PC is illustrated for a generic field variable, $\zeta(\boldsymbol{x}, t, \boldsymbol{\xi})$, which is decomposed according to:

$$(4.1) \qquad \zeta(\boldsymbol{x}, t, \boldsymbol{\xi}) = \sum_{i=0}^{P} \zeta_i(\boldsymbol{x}, t) \Psi_i(\boldsymbol{\xi}),$$

where $\boldsymbol{\xi} \equiv \xi_1, \ldots, \xi_{N_{KL}}$, the $\zeta_i$ are (yet to be determined) deterministic "coefficients", $\Psi_i$ denote the Polynomial Chaos [27, 1, 20], while $P + 1$ is the total number of modes used in the spectral expansion. The $\Psi_i$ are multi-dimensional orthogonal Hermite polynomials of the uncorrelated Gaussians [11]. Consistent with the notation introduced in [15], we shall denote by $No$ the order of polynomial expansion.

We rely on Eq. (4.1) to form representations of the thermodynamic pressure field as well as all field variables. For the purpose of computational convenience, however, the original form of the governing equations is first modified by differentiating the equation of state with respect to time, and combining with the energy equation. The resulting equation system is thus expressed as [25, 14]:

$$(4.2) \qquad \frac{\partial \rho}{\partial t} = \frac{1}{\gamma T} \frac{\partial \overline{P}}{\partial t} + \frac{1}{T} \left( \rho \boldsymbol{u} \cdot \boldsymbol{\nabla} T - \frac{1}{\mathrm{Pr}\sqrt{\mathrm{Ra}}} \boldsymbol{\nabla} \cdot (\kappa \boldsymbol{\nabla} T) \right)$$

$$(4.3) \qquad \frac{\partial \overline{P}}{\partial t} = -\gamma \frac{\int_\Omega \frac{1}{T} \left( \rho \boldsymbol{u} \cdot \boldsymbol{\nabla} T - \frac{1}{\mathrm{Pr}\sqrt{\mathrm{Ra}}} \boldsymbol{\nabla} \cdot (\kappa \boldsymbol{\nabla} T) \right) d\Omega}{\int_\Omega \frac{1}{T} d\Omega}$$

$$(4.4) \qquad \frac{\partial u}{\partial t} = -\frac{\partial(\rho u^2)}{\partial x} - \frac{\partial(\rho uv)}{\partial y} - \frac{\partial \Pi}{\partial x} + \frac{1}{\sqrt{\mathrm{Ra}}} \Phi_x$$

$$(4.5) \qquad \frac{\partial v}{\partial t} = -\frac{\partial(\rho uv)}{\partial x} - \frac{\partial(\rho v^2)}{\partial y} - \frac{\partial \Pi}{\partial y} + \frac{1}{\sqrt{\mathrm{Ra}}} \Phi_y - \frac{1}{\mathrm{Pr}} \frac{\rho - 1}{2\epsilon}$$

$$(4.6) \qquad T = \frac{\overline{P}}{\rho}$$

As in [24], the evolution equation for the thermodynamic pressure has been derived by enforcing global mass conservation over the whole domain.

Governing equations for the unknown expansion coefficients are obtained using a weighted residual approach, based on inserting the PC expansion into the modified system above, and taking the inner product with the PC basis [11, 16, 15]. Taking advantage of the orthogonality of the $\Psi_i$'s, we formally obtain:

$$(4.7) \qquad \frac{\partial \rho_k}{\partial t} = \mathcal{H}_k$$

$$(4.8) \qquad \frac{\partial \overline{P}_k}{\partial t} = \mathcal{G}_k$$

$$(4.9) \qquad \frac{\partial u_k}{\partial t} = \mathcal{X}_k - \frac{\partial \Pi_k}{\partial x}$$

$$(4.10) \qquad \frac{\partial v_k}{\partial t} = \mathcal{Y}_k - \frac{\partial \Pi_k}{\partial y}$$

$$(4.11) \qquad T_k = \left(\frac{\overline{P}}{\rho}\right)_k$$

where

$$(4.12) \qquad \mathcal{H}_k \equiv \frac{1}{\gamma}\left(\frac{1}{T}\frac{\partial \overline{P}}{\partial t}\right)_k + \left(\frac{1}{T}\left[\rho \boldsymbol{u}\cdot\boldsymbol{\nabla}T - \frac{1}{\Pr\sqrt{\mathrm{Ra}}}\boldsymbol{\nabla}\cdot(\kappa\boldsymbol{\nabla}T)\right]\right)_k$$

$$(4.13) \qquad \mathcal{G}_k \equiv -\gamma\left[\frac{\int_\Omega \frac{1}{T}\left(\rho\boldsymbol{u}\cdot\boldsymbol{\nabla}T - \frac{1}{\Pr\sqrt{\mathrm{Ra}}}\boldsymbol{\nabla}\cdot(\kappa\boldsymbol{\nabla}T)\right)d\Omega}{\int_\Omega \frac{1}{T}d\Omega}\right]_k$$

$$(4.14) \qquad \mathcal{X}_k \equiv -\frac{\partial\left(\rho u^2\right)_k}{\partial x} - \frac{\partial\left(\rho uv\right)_k}{\partial y} + \frac{1}{\sqrt{\mathrm{Ra}}}\left(\Phi_x\right)_k$$

$$(4.15) \qquad \mathcal{Y}_k \equiv -\frac{\partial\left(\rho uv\right)_k}{\partial x} - \frac{\partial\left(\rho v^2\right)_k}{\partial y} + \frac{1}{\sqrt{\mathrm{Ra}}}\left(\Phi_y\right)_k - \frac{1}{\Pr}\frac{\rho_k - 1}{2\epsilon}$$

and the subscripts $k$ refers to the mode index. The subsecript notation denoting mode indices is used both for variables and experessions; in the latter case, we have

$$(\mathcal{E})_k \equiv \frac{\langle(\mathcal{E})\Psi_k\rangle}{\langle\Psi_k^2\rangle}$$

where $(\mathcal{E})$ denotes a generic expression.

**4.2. Boundary Conditions.** The weighted residual procedure is also used to derive boundary conditions for the mode strength. Specifically, the PC decomposition is also introduced into the corresponding expressions, and orthogonal projections are used to derive boundary conditions for the velocity and temperature modes. We obtain:

$$(4.16) \qquad \boldsymbol{u}_k = 0, \quad k = 0,\ldots,P \qquad \forall \boldsymbol{x} \in \partial\Omega$$

$$(4.17) \qquad \frac{\partial T_k}{\partial y} = 0, \quad k = 0,\ldots,P \quad \text{for } y = 0, \text{and } y = 1$$

$$(4.18) \qquad T_0(x = 0, y) = 1 + \epsilon, \qquad T_0(x = 1, y) = 1 - \epsilon$$

$$(4.19) \quad T_k(x = 0, y) = 0, \quad T_k(x = 1, y) = \epsilon\sqrt{\lambda_k}f_k(y) \qquad \text{for } k = 1,\ldots,N_{KL}$$

$$(4.20) \qquad T_k(x = 0, y) = T_k(x = 1, y) = 0 \qquad \text{for } k > N_{KL}$$

Here $\Omega = [0,1] \times [0,1]$ denotes the computational domain, and $\partial\Omega$ is its boundary.

**4.3. Solution Method.** The solution scheme is adapted from the variable density projection method developed in [25, 14]. For spatial discretization, we rely on a uniform, Cartesian, staggered grid with $N_x$ and $N_y$ cells in the $x$ and $y$ directions respectively. Velocity components are specified at cell edges, while scalar variables are defined at cell centers. Second-order conservative centered differences are used to approximate spatial derivatives.

For the present setup, an explicit time integration scheme proves suitable. We use the second-order Adams-Bashforth scheme to update the density field and thermodynamic pressure, according to:

$$(4.21) \qquad \rho_k^{n+1} = \rho_k^n + \Delta t \left( \frac{3}{2} \mathcal{H}_k^n - \frac{1}{2} \mathcal{H}_k^{n-1} \right) , \quad k = 0, \ldots, P$$

$$(4.22) \qquad \overline{P}_k^{n+1} = \overline{P}_k^n + \Delta t \left( \frac{3}{2} \mathcal{G}_k^n - \frac{1}{2} \mathcal{G}_k^{n-1} \right) , \quad k = 0, \ldots, P$$

where $\Delta t$ denotes the time step and superscripts refer to the time level. Using the updated density field and thermodynamic pressure, the temperature is updated using the equation of state:

$$(4.23) \qquad T_k^{n+1} = \left( \frac{\overline{P}}{\rho} \right)_k^{n+1} , \quad k = 0, \ldots, P$$

Next, we integrate the pressure-split momentum equation using:

$$(4.24) \qquad (\rho u)_k^* = (\rho u)_k^n + \Delta t \left( \frac{3}{2} \mathcal{X}_k^n - \frac{1}{2} \mathcal{X}_k^{n-1} \right) , \quad k = 0, \ldots, P$$

$$(4.25) \qquad (\rho v)_k^* = (\rho v)_k^n + \Delta t \left( \frac{3}{2} \mathcal{Y}_k^n - \frac{1}{2} \mathcal{Y}_k^{n-1} \right) , \quad k = 0, \ldots, P$$

As in the SPM introduced in [16, 15], the pressure field is then obtained by inverting the following **decoupled** elliptic systems for the pressure modes:

$$(4.26) \qquad \nabla^2 \Pi_k = \frac{1}{\Delta t} \left[ \boldsymbol{\nabla} \cdot (\rho \boldsymbol{u})_k^* + \left. \frac{\partial \rho_k}{\partial t} \right|^{n+1} \right] , \quad k = 0, \ldots, P$$

with homogeneous boundary Neumann conditions on all the modes. In Eq. (4.26), the time derivative is obtained from the second-order difference:

$$(4.27) \qquad \left. \frac{\partial \rho_k}{\partial t} \right|^{n+1} = \frac{3 \rho_k^{n+1} - 4 \rho_k^n + \rho_k^{n-1}}{\Delta t} , \quad k = 0, \ldots, P$$

A pressure correction step is then implemented in order to enforce local continuity constraints:

$$(4.28) \qquad (\rho u)_k^{n+1} = (\rho u)_k^* - \Delta t \frac{\partial \Pi_k}{\partial x} , \quad k = 0, \ldots, P$$

$$(4.29) \qquad (\rho v)_k^{n+1} = (\rho v)_k^* - \Delta t \frac{\partial \Pi_k}{\partial y} , \quad k = 0, \ldots, P$$

and the updated velocity field is finally obtained from:

$$(4.30) \qquad u_k^{n+1} = \left( \frac{(\rho u)^{n+1}}{\rho^{n+1}} \right)_k , \quad k = 0, \ldots, P$$

$$(4.31) \qquad v_k^{n+1} = \left( \frac{(\rho v)^{n+1}}{\rho^{n+1}} \right)_k , \quad k = 0, \ldots, P$$

**4.4. Galerkin and Pseudo-Spectral Evaluation of Non-Linear Terms.**
Unlike the system of equations appearing in the Boussinesq limit, the above system
involves various non-linear combinations of stochastic quantities. The latter include
quadratic and higher-order products, as well as inverse functions involving tempera-
ture or density.

For quadratic products, the weighted residual approach can be easily implemented
in its true Galerkin form. For instance, the product of $c = ab$ of two stochastic
quantities $a$ and $b$ can be directly evaluated using [16, 15]:

$$(4.32) \qquad c_k = \sum_{i=0}^{P} \sum_{j=0}^{P} C_{ijk} a_i b_j, \quad k = 0, \ldots, P$$

where $C_{ijk}$ is the (sparse) tensor given by:

$$(4.33) \qquad C_{ijk} = \frac{\langle \Psi_i \Psi_j \Psi_k \rangle}{\langle \Psi_k^2 \rangle}$$

for $0 \le i, j, k \le P$.

For cubic and higher order products, the Galerkin procedure becomes compu-
tationally cumbersome and inefficient. On one hand, it requires the evaluation and
storage of higher-rank tensors. While still possible, these tensors are generally less
sparse than $C_{ijk}$, resulting in higher storage and CPU requirements.

In order to avoid the above drawback, a pseudo-spectral approach is developed for
non-linear expressions [13]. For product expressions involving more than two stochas-
tic quantities, we resort to repeated applications of "binary" Galerkin evaluations.
For example, for the triple product $d = abc$, a two step approach is utilized, where
we first compute $d' = ab$ using Eq. (4.32), and then apply the same formula to obtain
$d = d'c$. This approach is immediately generalized to products involving an arbitrary
number of stochastic quantities.

The only remaining non-linear expressions involve inverse operations (of temper-
ature or density). Unless otherwise noted, these expressions are approximated using
a truncated Taylor series expansion around the mean of the stochastic quantity. For
instance, the inverse $1/a$ of a stochastic quantity $a = \sum_{i=0}^{P} a_i \Psi_i$ is approximated as:

$$(4.34) \qquad \frac{1}{a} \simeq \frac{1}{a_0} - \frac{1}{a_0^2}(a - a_0) + \frac{1}{a_0^3}(a - a_0)^2 - \frac{1}{a_0^3}(a - a_0)^3 + \cdots$$

where the higher order exponentiations are evaluated using the pseudo-spectral ap-
proach just introduced.

Note that, as expected, the pseudo-spectral evaluation of stochastic quantities
introduces aliasing errors. When the spectral representation is sufficiently resolved,
however, these errors do not degrade the spectral convergence of the scheme. This
claim may be verified by systematic refinement of the representation, as performed
for instance in [15]. In the present computations most of the common operations
involving stochastic quantities (including those outlined above) are evaluated using a
UQ toolkit that contains subroutines for individual operations [8, 13].

**4.5. Pressure Solvability Constraints.** In the development of the above stochas-
tic solver, one unanticipated difficulty arose during the enforcement of stochastic di-
vergence constraints associated with the pressure Poisson equation. As reflected in
Eq. (4.26), the pressure modes are obtained as the solution of Poisson equations with

homogeneous Neumann conditions. These equations are thus subject to the following solvability constraints:

$$(4.35) \qquad \int_\Omega \frac{1}{\Delta t} \left[ \boldsymbol{\nabla} \cdot (\rho \boldsymbol{u})_k^* + \left. \frac{\partial \rho_k}{\partial t} \right|^{n+1} \right] d\Omega = 0$$

For a closed domain with rigid boundaries, the divergence term appearing in the integral vanishes identically, both in the continuous limit and for the present staggered discretization. Thus, the only remaining concern is the annihilation of the second term, in other words exact enforcement of global mass conservation over the entire domain.

Unfortunately, the right hand side density evolution equation (4.7) involves complex combinations of stochastic quantities which, as mentioned earlier, are only approximately estimated. Consequently, without special care, the solvability constraints could only be approximately satisfied. Even though errors associated with solvability constraints were generally minute, these always led to the blow-up of the computations.

In order to overcome these difficulties, special care in the evaluation of the thermodynamic pressure source term was implemented. The procedure is based on rewriting Eq. (4.13) as:

$$(4.36) \qquad \mathcal{T}\mathcal{G} = \mathcal{S}$$

where $\mathcal{G}$ refers to the stochastic quantity with coefficients $(\mathcal{G}_1, \ldots, \mathcal{G}_k)$,

$$(4.37) \qquad \mathcal{T}_k \equiv \int_\Omega \left[ \frac{1}{T} \right]_k d\Omega$$

and

$$(4.38) \qquad \mathcal{S}_k = \int_\Omega \left[ \frac{1}{T} \left( \rho \boldsymbol{u} \cdot \boldsymbol{\nabla} T - \frac{1}{\mathrm{Pr}\sqrt{\mathrm{Ra}}} \boldsymbol{\nabla} \cdot (\kappa \boldsymbol{\nabla} T) \right) \right]_k d\Omega$$

Next, instead of using the approximate Taylor series approach (4.34) to determine $\mathcal{G}$, the latter is obtained by inverting the linear system:

$$(4.39) \qquad \sum_{i=0}^{P} \sum_{j=0}^{P} C_{ijk} \mathcal{T}_i \mathcal{G}_j = \mathcal{S}_k, \quad k = 0, \ldots, P$$

which may be alternatively written as:

$$(4.40) \qquad \mathbf{A}\mathcal{G} = \mathcal{S}$$

where $\mathbf{A}$ is the matrix given by:

$$(4.41) \qquad A_{ij} = \sum_{k=0}^{P} C_{ijk} \mathcal{T}_k, \quad 0 \le i, j \le P$$

It is readily verified that when the $\mathcal{G}_k$'s are obtained as the solution of the above equation the integral constraints in Eq. (4.35) are exactly satisfied. (To this end, it is sufficient to note that the above inverse procedure is an exact (discrete) de-convolution of the Galerkin product.) Furthermore, with the resulting scheme, stable numerical solutions are obtained. Thus, the present approach provides a simple and effective means for obtaining a pressure solution that ensures that local divergence constraints are satisfied.

## 5. Validation of the Numerical Solver.

**5.1. Boussinesq Limit.** As a first validation, the results obtained with the spectral solver are compared with previous stochastic spectral computations reported in [15] for the Boussinesq limit. For clarity of the presentations, the quantities given in this subsection are re-scaled consistently with the Boussinesq normalization.

**5.1.1. Zero order spectral expansion.** We set $\epsilon = 0.001$, and use the temperature independent properties ($\kappa = \mu = 1$). Then the grid convergence of the solution is analyzed for increasingly refined spatial discretization, and zero order spectral expansion (i.e. the deterministic problem). Results are reported in Table 5.1, for Ra $= 10^6$, in terms of wall-averaged Nusselt number together with its minimal and maximal values along the vertical walls, respectively:

$$(5.1)\ \mathrm{Nu_{av}} = \frac{1}{2\epsilon}\int_0^1 -\kappa\frac{\partial \mathrm{T}(0,\mathrm{y})}{\partial \mathrm{x}}\mathrm{dy}, \quad \mathrm{Nu_{min,max}} = \frac{1}{2\epsilon}\min,\max\left(-\kappa\frac{\partial \mathrm{T}(0,\mathrm{y})}{\partial \mathrm{x}}\right).$$

Note that these quantities are computed along the hot wall; for the present small value of $\epsilon$, the solution is nearly symmetrical with respect to the central vertical plane. In fact, the agreement between hot and cold walls values is within 0.1% for the minima and maxima of the Nusselt, while the wall-averaged Nusselt numbers on both walls are equal (for any $\epsilon$) at steady state. Table 5.1 shows that as the grid is refined, the present finite difference results rapidly approach the spectral results of Le Quéré [17]. Moreover, a detailed analysis of the solution (not shown) shows that the temperature and velocity fields are also in very good agreement with the results reported in [17]. In Table 5.2, we compare the computed values of the wall-averaged Nusselt number at Ra $= 10^5$, $\epsilon = 0.001$, obtained using a $80 \times 80$ grid, with some reference results based on the Boussinesq approximation. Again, a good agreement with reported results is observed.

| $N_x \times N_y$ | $40 \times 40$ | $80 \times 80$ | $120 \times 120$ | $160 \times 160$ | spectral [17] |
|---|---|---|---|---|---|
| $\mathrm{Nu_{av}}$ | 9.426 | 8.982 | 8.895 | 8.865 | 8.825 |
| $\mathrm{Nu_{min}}$ | 0.939 | 0.971 | 0.976 | 0.978 | - |
| $\mathrm{Nu_{max}}$ | 20.50 | 18.74 | 18.09 | 17.85 | - |

TABLE 5.1

*Mean, minimum and maximum Nusselt numbers for different spatial discretizations with $\epsilon = 0.001$ and Ra $= 10^6$. Deterministic results are obtained using the stochastic code with 0-order spectral expansion with a constant-property model.*

| | Model | $\mathrm{Nu_{av}}$ | $\mathrm{Nu_{min}}$ | $\mathrm{Nu_{max}}$ |
|---|---|---|---|---|
| De Vahl Davis [7] | Boussinesq | 4.519 | 0.729 | 7.717 |
| Le Quéré *et al.* [18] | Boussinesq | 4.523 | 0.728 | 7.720 |
| Chenoweth *et al.* [2] | Boussinesq | 4.520 | - | - |
| Hortmann *et al.* [12] | Boussinesq | 4.522 | - | 7.720 |
| Paillere *et al.* [26] (80x80) | zero-Mach ($\epsilon = 0.01$) | 4.523 | 0.738 | 7.68 |
| Present (80x80) | zero-Mach ($\epsilon = 0.001$) | 4.547 | 0.726 | 7.840 |

TABLE 5.2

*Wall-averaged, minimum and maximum Nusselt numbers, at Ra $= 10^5$. Results are compared with reported Boussinesq predictions. The present zero-Mach-number, deterministic results were obtained using $\epsilon = 0.001$, constant-property model on a $80 \times 80$ uniform grid.*

**5.1.2. Stochastic Boussinesq computations.** The predictions of the stochastic zero-Mach code for small $\epsilon$ are now validated against the spectral Boussinesq computations presented in [15]. Results are obtained with $L_c = 1$ and $\sigma_T = 0.5$. The random temperature fluctuations are represented using a KL expansion with $N_{KL} = 4$, and a second-order PC expansion is used. Accordingly, $P = 14$ i.e. the PC expansion has 15 polynomials.

In order to compare the zero-Mach stochastic predictions with Boussinesq results [15], we choose a small value of the Boussinesq parameter, $\epsilon = 0.001$. The constant-property formulation is used, and the governing equations are time-integrated up to steady state, using 80×80 and 140×100 grids. As shown in Table 5.3, when the same spatial grid resolution is used, there is excellent agreement between the Boussinesq [15] and zero-Mach predictions of the mean Nusselt number, $\langle Nu_{av} \rangle$ and its standard deviation, $\sigma(Nu_{av})$. Specifically, for a 140×100 grid, the differences between the zero-Mach and Boussinesq predictions are less than 0.15%, while differences between the zero-Mach predictions at different resolution levels are less than 1.6%. The higher value of $< Nu_{av} >$ for the lower grid resolution is not surprising, as the convergence analysis provided above (Table 5.1) has shown an increasing over-estimation of $Nu_{av}$ with decreasing grid resolution for the deterministic case. In addition to the comparison in Table 5.3, detailed analysis (not shown) of the individual modes in the spectral expansion also reveals excellent agreement between zero-Mach and Boussinesq predictions. In particular, when the same grid resolution is used, the relative difference between corresponding second-order modes in the Boussinesq and zero-Mach solutions is everywhere less than 1%. Thus, at small $\epsilon$, close agreement between the zero-Mach and Boussinesq predictions is observed both for integral quantities and local field values.

|  | N.B. 80×80 | N.B. 140×100 | Boussinesq 140×100 |
|---|---|---|---|
| $< Nu_{av} >$ | 9.0794 | 8.9716 | 8.9729 |
| $\sigma(Nu_{av})$ | 2.4993 | 2.4602 | 2.4632 |

TABLE 5.3

*Comparison of zero-Mach stochastic spectral computations for $\epsilon = 0.001$ with Boussinesq predictions from [15].*

**5.2. Non-Boussinesq regime.** In this section we examine the behavior of the zero-Mach code in the non-Boussinesq regime, i.e. for moderate values of $\epsilon$. Since, to our knowledge, no results are available for the stochastic problem, the analysis is limited to the deterministic case. The effects of the Boussinesq parameter $\epsilon$ on the flow statistics in the stochastic case are examined in the following section.

| $N_x \times N_y$ | $40 \times 40$ | $80 \times 80$ | $120 \times 120$ | $160 \times 160$ |
|---|---|---|---|---|
| $Nu_{av}$ | 8.600 | 8.744 | 8.688 | 8.651 |
| $Nu_{min}$-(hot/cold) | (0.987-2.037) | (1.057-0.663) | (1.064-0.677) | (1.064-0.691) |
| $Nu_{max}$-(hot/cold) | (23.86-12.48) | (21.81-14.77) | (21.00-15.38) | (20.70-15.48) |

TABLE 5.4

*Mean, minimum and maximum Nusselt numbers on the hot and cold walls for different spatial discretizations. Deterministic predictions obtained using $\epsilon = 0.6$, $Ra = 10^6$ and a variable-property model.*

We start with a brief examination of the effects of spatial resolution on steady-

state predictions. To this end, we set $\epsilon = 0.6$, Ra $= 10^6$ and rely on the variable-property model. In Table 5.4, the steady-state Nusselt number is computed with spatial resolutions, corresponding to grids with $40\times40$, $80\times80$, $120\times120$, and $160\times160$ cells. Also shown are the maximum and minimum values of Nu on the hot and cold walls. Note that for this large $\epsilon$ case, the local heat flux distributions on the hot and cold walls differ, which leads to corresponding maximum and minimum values. However, at steady state the wall-averaged Nusselt number is identical for both the hot and cold walls. The results of Table 5.4 also show that as the grid is refined, the predictions tend towards a fixed value. In particular, when the number of cells along each direction is larger or equal to 80, the predicted values of $\mathrm{Nu_{av}}$ vary by less than 1%.
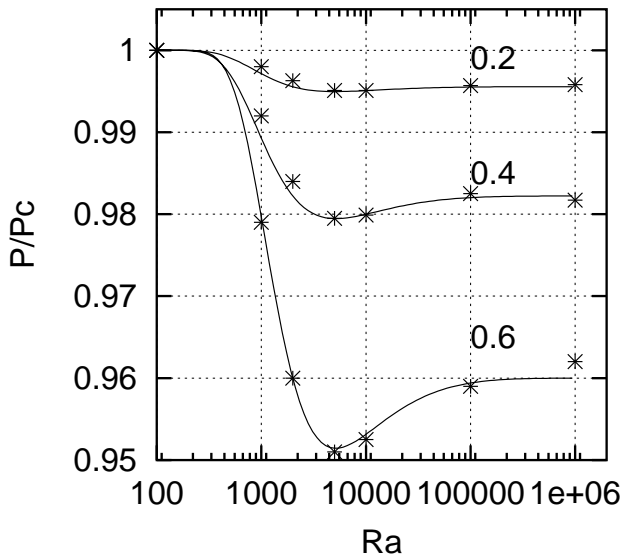


FIG. 5.1. *Computed values of $\overline{P}/\overline{P}_c$ (symbols) for different values of the Rayleigh number, Ra, and the Boussinesq parameter, $\epsilon = 0.2$, $0.4$ and $0.6$. Solid lines reflect the analytical results of [2]. A computational grid with $80 \times 80$ cells is used.*

In order to gain additional confidence in the computations, we contrast the predicted value of the steady-state thermodynamic pressure, $\overline{P}$, with the analytical predictions of Chenoweth & Paolucci [2]. This is a stringent test because the steady-state pressure is obtained by time integration of the unsteady pressure field (Eq. 4.3), and is thus potentially affected by the accumulation of time integration errors. Several investigations (e.g. [2, 19, 26]) have in fact pointed out to severe difficulties in computing the static pressure by direct integration, due to inaccurate time integration schemes and/or inconsistency of the overall scheme. For the present scheme, however, the steady $P$ is accurately predicted, as illustrated in Fig. 5.1. The latter depicts curves of $\overline{P}(\epsilon)/\overline{P}_c(\epsilon)$, where $\overline{P}$ is the steady pressure and $\overline{P}_c$ is the pressure corresponding to a purely conductive solution [2]. Results are generated for $\epsilon = 0.2$, 0.4, 0.6 and Rayleigh numbers in the range $10^2 \leq \mathrm{Ra} \leq 10^6$. The simulations were performed on a $80 \times 80$ grid using the variable-property model. In each case, the numerical time-steps was selected so as to satisfy the stability constraints of the explicit time integration scheme. In the figure, the static pressures computed at Ra $= 10^2$ were

used to estimate $P_c(\epsilon)$, since they were found to be in excellent agreement with the analytical expressions of [2]. As shown in Fig. 5.1, an excellent agreement with the analytical results [2] is obtained, but small deviations are observed at $Ra = 10^6$ and $\epsilon = 0.6$ where the grid may not be sufficiently refined.

**6. Effect of the Boussinesq parameter on uncertainty .** Following the brief validation study above, the stochastic zero-Mach-number code is applied in this section to analyze the effect of the Boussinesq parameter on the statistics of the stochastic cavity flow. We set $Ra = 10^6$, $L_c = 1$, $\sigma_T = 0.5$, and consider four different values of $\epsilon$, $\epsilon = 0.01$, 0.1, 0.2, and 0.3. We rely on previous experiences in [15] and restrict the computations to a second-order PC expansion, and perform computations on a grid with $N_x = 120$ and $N_y = 100$. For brevity, only the constant-property model is used.

**6.1. Heat transfer characteristics.** In order to compare the solutions for different values of the Boussinesq parameter, including the Boussinesq regime at very small $\epsilon$, it is convenient to rescale the temperature modes according to:

$$T_0 \longrightarrow \theta_0 \equiv 1 + \frac{T_0 - 1}{2\epsilon}$$
$$T_k \longrightarrow \theta_k \equiv \frac{T_k}{2\epsilon} \quad k = 1, \ldots, P.$$

Based on this normalization, the wall-averaged and local Nusselt numbers are given by:

$$(6.1) \; \mathrm{Nu}_{av}(\boldsymbol{\xi}) = -\sum_{k=0}^{P} \int_0^1 \frac{\partial \theta_k}{\partial x}(x, y)\Psi_k(\boldsymbol{\xi})dy, \quad \mathrm{Nu}(y, \boldsymbol{\xi}) = -\sum_{k=0}^{P} \frac{\partial \theta_k}{\partial x}(x, y)\Psi_k(\boldsymbol{\xi}).$$

with $x = 0$ for the hot wall and $x = 1$ for the cold wall. As mentioned earlier, the local values of $\mathrm{Nu}(y)$ may differ on both walls, but the average values are equal at steady state.

| | $No = 1$ | | | | $No = 0$ |
|---|---|---|---|---|---|
| | $\langle \mathrm{Nu}_{av}\rangle$ | $\sigma(\mathrm{Nu}_{av})$ | $< \overline{P} >$ | $\sigma(\overline{P})$ | $\mathrm{Nu}_{av}$ |
| $\epsilon = 0.01$ | 8.990 | 2.479 | 0.9999 | 0.0022 | 8.871 |
| $\epsilon = 0.10$ | 9.018 | 2.531 | 0.9959 | 0.0232 | 8.872 |
| $\epsilon = 0.20$ | 9.055 | 2.591 | 0.9833 | 0.0501 | 8.874 |
| $\epsilon = 0.30$ | 9.103 | 2.653 | 0.9612 | 0.0819 | 8.880 |
| | $No = 2$ | | | | $No = 0$ |
| | $\langle \mathrm{Nu}_{av}\rangle$ | $\sigma(\mathrm{Nu}_{av})$ | $< \overline{P} >$ | $\sigma(\overline{P})$ | $\mathrm{Nu}_{av}$ |
| $\epsilon = 0.01$ | 8.992 | 2.472 | 0.9999 | 0.0022 | 8.871 |
| $\epsilon = 0.10$ | 9.019 | 2.529 | 0.9959 | 0.0232 | 8.872 |
| $\epsilon = 0.20$ | 9.058 | 2.598 | 0.9832 | 0.0538 | 8.874 |
| $\epsilon = 0.30$ | 9.108 | 2.676 | 0.9609 | 0.0829 | 8.880 |

TABLE 6.1

*Expectations $(< . >)$ and standard deviations $(\sigma(.))$ of the Nusselt numbers and normalized thermodynamic pressure $\overline{P}$, for different $\epsilon$ using first- and second-order expansions. The Nusselt number for the deterministic case (zero-order expansion) is also given in the last column.*

In Table 6.1, the expected values and standard deviations of $\mathrm{Nu}_{av}$ and $\overline{P}$ at steady state are given for $\epsilon = 0.01$, 0.1, 0.2 and 0.3, for the spectral solutions obtained using

first- and second-order PC expansions, $No = 1$ and 2 respectively. The results show that $< \mathrm{Nu_{av}} >$ and $\sigma(\mathrm{Nu_{av}})$ increase with $\epsilon$. The results also show that the first-order and second-order PC expansions yield estimates of $< \mathrm{Nu_{av}} >$ that are in close agreement, but differences in the corresponding standard deviations can be noted. For $\epsilon \leq 0.1$, the first-order PC expansion slightly overestimates $\sigma(\mathrm{Nu_{av}})$, while the reverse trend occurs at higher $\epsilon$. Table 6.1 also shows that the mean thermodynamic pressure and its standard deviation exhibit a non-linear dependence on $\epsilon$. The differences between first and second-order PC predictions are more pronounced than for the Nusselt number. In particular, for $\epsilon \geq 0.2$, a second-order PC expansion is found necessary for accurate prediction of the standard deviation of the thermodynamic pressure.

|  | Hot wall | | Cold wall | |
|---|---|---|---|---|
|  | $min \langle \mathrm{Nu} \rangle$ | $max \langle \mathrm{Nu} \rangle$ | $min \langle \mathrm{Nu} \rangle$ | $max \langle \mathrm{Nu} \rangle$ |
| $\epsilon = 0.01$ | 0.981 | 18.50 | 0.917 | 18.41 |
| $\epsilon = 0.10$ | 0.999 | 18.82 | 0.890 | 18.30 |
| $\epsilon = 0.20$ | 1.019 | 19.24 | 0.853 | 18.21 |
| $\epsilon = 0.20$ | 1.041 | 19.76 | 0.803 | 18.17 |
|  | $min[\sigma(\mathrm{Nu})]$ | $max[\sigma(\mathrm{Nu})]$ | $min[\sigma(\mathrm{Nu})]$ | $max[\sigma(\mathrm{Nu})]$ |
| $\epsilon = 0.01$ | 0.244 | 5.559 | 0.805 | 6.358 |
| $\epsilon = 0.10$ | 0.255 | 5.871 | 0.816 | 6.540 |
| $\epsilon = 0.20$ | 0.268 | 6.302 | 0.834 | 6.814 |
| $\epsilon = 0.20$ | 0.282 | 6.831 | 0.866 | 7.228 |

TABLE 6.2

*Local heat-flux statistics along the hot and cold walls. Provided are the minima and maxima of the standard deviation of the local heat flux for different values of $\epsilon$. Results were obtained using a second-order polynomial expansion.*
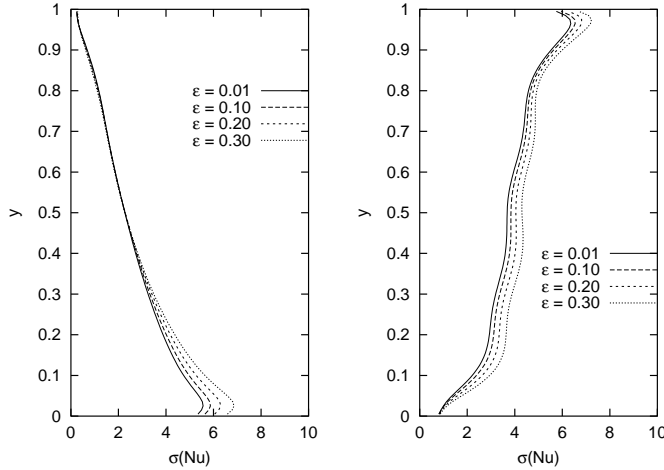


FIG. 6.1. *Standard deviation of the local heat flux across the hot (left plot) and cold (right plot) walls. Results were obtained using a second-order PC with $N_{KL} = 4$ and a constant-property model.*

The results presented in Table 6.1 provide information on the effect of $\epsilon$ of the statistics of the overall heat transfer. We now turn our attention to the statistics of the local heat flux distributions on the hot and cold walls. Provided in Table 6.2 are

the minima and maxima of the mean heat flux and its standard deviation for both the hot and cold walls. The results indicate that there are opposite trends with $\epsilon$ concerning the maxima and minima of $< \mathrm{Nu} >$ on the two walls. Specifically, the minimum and maximum of values of $< \mathrm{Nu} >$ increase with increasing $\epsilon$ on the hot wall, while they decrease with increasing $\epsilon$ on the cold wall. In addition, the effect of $\epsilon$ on the maximum expected heat flux is more pronounced on the hot wall than it is on the cold wall. Meanwhile, the maximum and minimum values of $\sigma(\mathrm{Nu})$ increase with $\epsilon$ on both the hot and cold walls. This trend is consistent with our previous observation that the standard deviation increases with $\epsilon$. It is also interesting to note that, as shown in Fig. 6.1, the values of $\sigma(\mathrm{Nu})$ are generally larger on the cold wall, where the uncertainty is applied, than on the hot wall. In addition, the figure shows that on the cold wall $\sigma(\mathrm{Nu})$ is everywhere affected by $\epsilon$, while on the hot wall the variations of $\sigma(\mathrm{Nu})$ with $\epsilon$ are limited to the lower part of the wall.
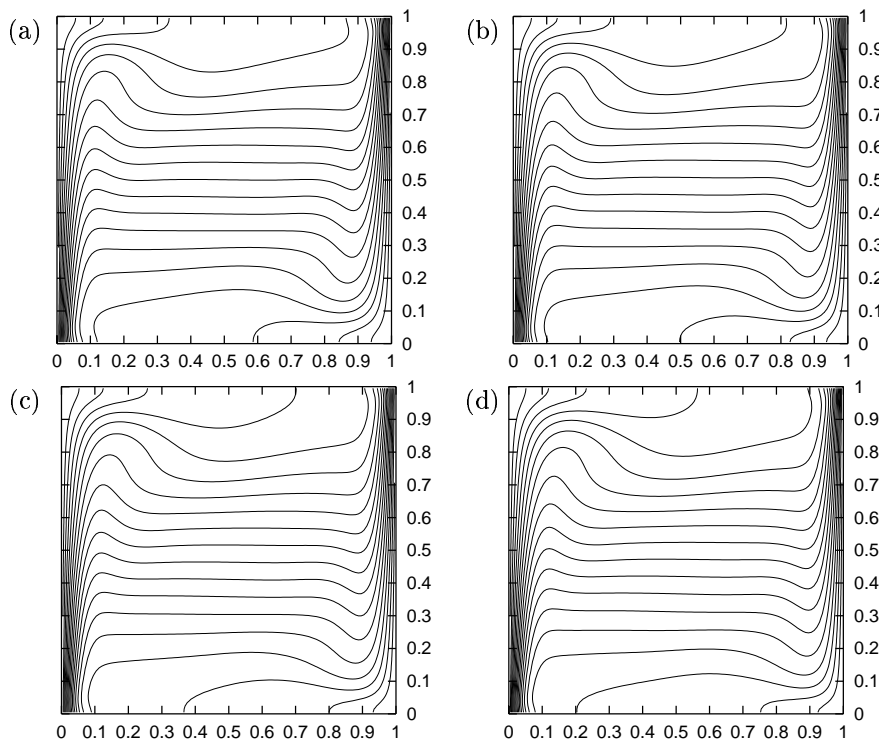


FIG. 6.2. *Contours of the mean scaled temperature $\theta$ for: (a) $\epsilon = 0.01$, (b) $\epsilon = 0.1$, (c) $\epsilon = 0.2$, and (d) $\epsilon = 0.3$. Contours range from the maximum value ($\theta = 1.5$) for the hot wall ($x = 0$) to the minimum ($\theta = 0.5$) on the cold wall ($x = 1$) with increments 0.05.*

**6.2. Mean fields.** In this section we examine the dependence of the mean temperature and velocity fields within the cavity on $\epsilon$. In Fig 6.2, the mean rescaled temperature fields $\theta_0$ are plotted for $\epsilon = 0.01$, $0.1$, $0.2$ and $0.3$. Thanks to the scaling, in all cases $\theta_0 = 1.5$ on the left(hot) wall, $\theta_0 = 0.5$ on the right (cold) wall. Thus, direct comparison for different $\epsilon$ is possible.

Figure 6.2 shows that the impact of $\epsilon$ on the scaled temperature field is essentially noticeable at the lower part of the and upper parts of the cavity. The effects are most pronounced around the upper left corner of the cavity near the hot wall and the lower
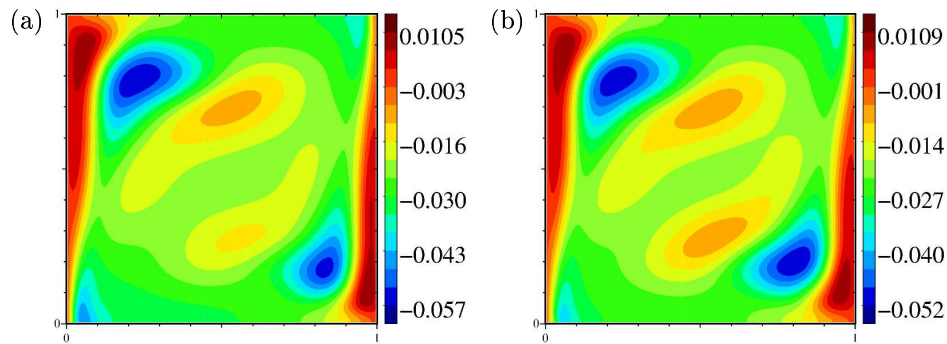
FIG. 6.3. *Contours of differences in scaled temperature fields:* (a) $< \theta(\epsilon = 0.3) > - < \theta(\epsilon = 0.01) >$ *for the second order polynomial expansion;* (b) $\theta(\epsilon = 0.3) - \theta(\epsilon = 0.01)$ *for the deterministic problem (0-order expansion).*
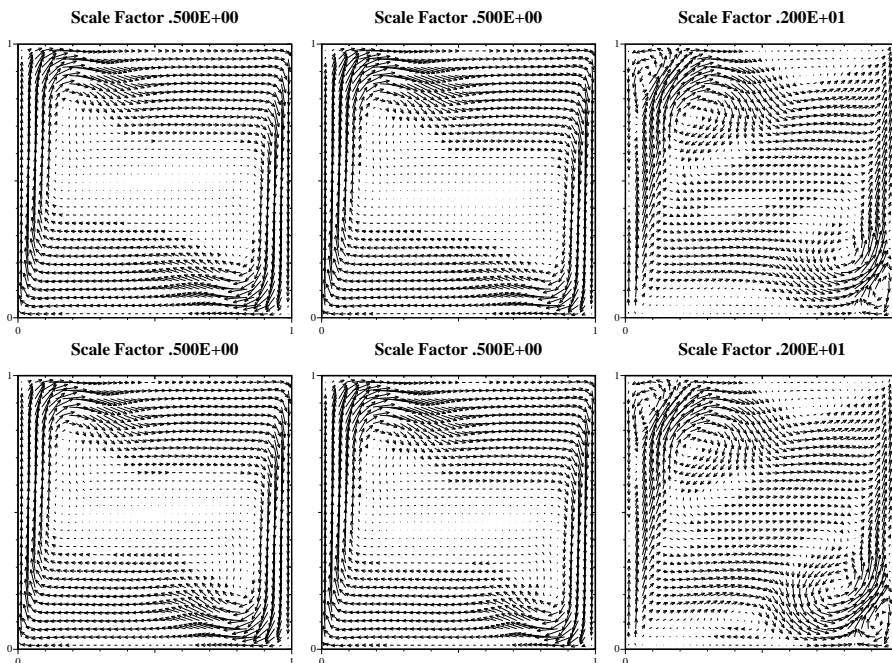


FIG. 6.4. *Top row: Mean velocity field for $\epsilon = 0.01$ (left), $\epsilon = 0.3$ (center) and the corresponding difference field (right). Results are obtained using a second-order PC expansion. Bottom row: Deterministic velocity field for $\epsilon = 0.01$ (left), $\epsilon = 0.3$ (center) and the corresponding difference field (right).*

right corner of the cavity near the cold wall. With increasing $\epsilon$ the fluid traveling at the bottom of the cavity has, on the mean, a lower scaled temperature; the same trend applies in the upper part of the cavity. In the core of the flow, the scaled temperature distributions exhibit similar shape for all $\epsilon$, reflecting the classical patterns of natural convection in a square cavity. In this region, the mean thermal stratification ($\partial \theta_0 / \partial y$) is weakly dependent on $\epsilon$.

To further analyze the influence of $\epsilon$ on $\theta_0$, in Fig. 6.3(a) we plot the difference

between the two averaged fields computed for $\epsilon = 0.01$ and 0.3. From this plot, one can observe that on average the scaled temperature in the cavity is globally lower for $\epsilon = 0.3$ than for $\epsilon = 0.01$, except along the two vertical boundary layers where it is higher. The figure also reveals that large temperature differences, with amplitude as high as 5% of $\Delta T$, occur in the neighborhood of the top left corner and bottom right corner. The difference in mean solutions should not be fully attributed to a different response to the temperature boundary condition uncertainty. To establish this claim, Fig. 6.3(b) shows the differences in scaled temperature fields, for the same values $\epsilon$, between deterministic computations. The similarity between the two frames in Fig. 6.3 indicates that imposition of stochastic conditions result, on average, in only weak amplification of the differences that occur in the deterministic solution. Similar observations can be drawn by inspection of the mean and deterministic velocity fields plotted in Fig. 6.4. Note the strong spatial correlation of the differences between the solution for $\epsilon = 0.01$ and 0.3 for the scaled temperature and velocity fields.
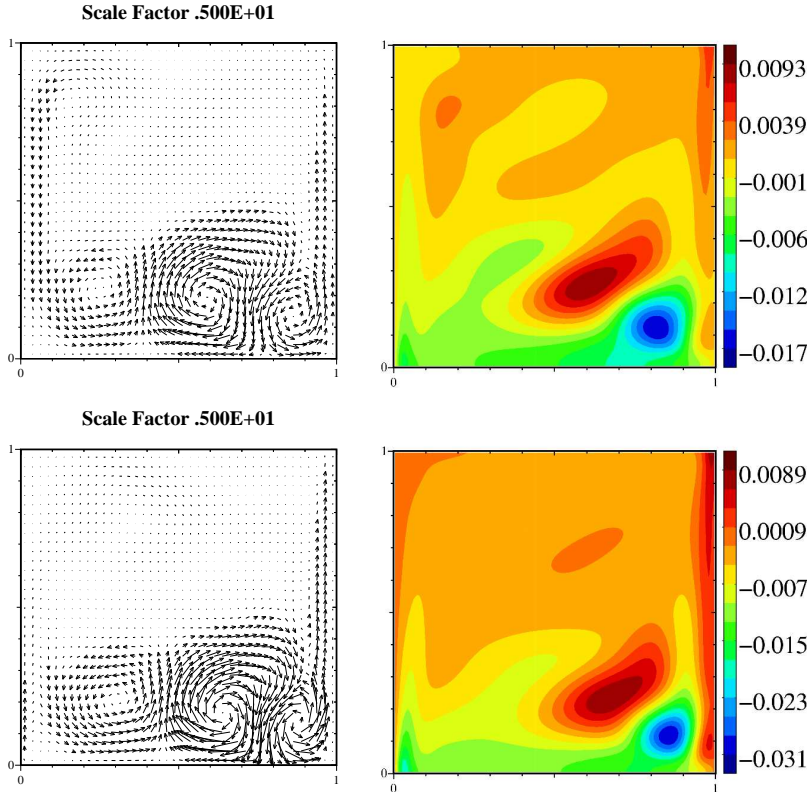


FIG. 6.5. *Differences between mean and deterministic velocity (left) and temperature (right). Top row: $\epsilon = 0.01$; bottom row: $\epsilon = 0.3$.*

It follows from the discussion above that the influence of $\epsilon$ on the mean solutions in the stochastic case is better understood when the corresponding deterministic, or zero order, solutions are first subtracted from the averaged fields. Results of such exercise are given in Fig. 6.5, based on second-order PC computations for $\epsilon = 0.3$ and $\epsilon = 0.01$. There are striking similarities between the distributions for both values of $\epsilon$. Specifically, for both cases the differences in the velocity fields exhibit three recircu-

lation zones, with alternated sign of circulation, along the lower wall. The strengths of these structures, which have been observed in the Boussinesq analysis [15], are amplified with increasing $\epsilon$. A similar effect is also visible for the scaled temperature fields plotted in Fig. 6.5. With respect to the deterministic solution, the application of stochastic conditions results in lower mean temperature at the bottom of the cavity, with a maximum amplitudes of less than 1.8% for $\epsilon = 0.01$ and greater than 3% for $\epsilon = 0.3$. Thus, the impact of stochastic temperature fluctuations exhibits a non-linear dependence on the Boussinesq parameter.
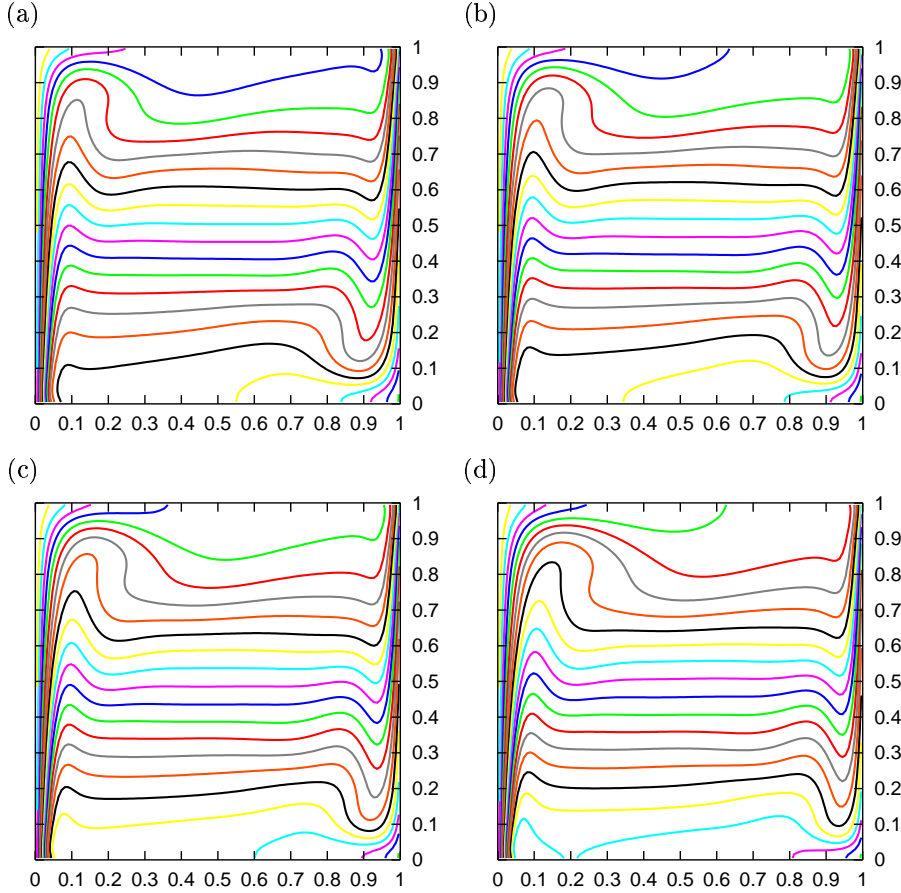


FIG. 6.6. *Standard deviation in scaled temperature $\theta$ for (a) $\epsilon = 0.01$, (b) $\epsilon = 0.1$, (c) $\epsilon = 0.2$, and (d) $\epsilon = 0.3$. Note that $\sigma_\theta = 0$ on the hot-wall ($x = 0$), where a deterministic temperature is imposed, and that it peaks on the cold wall ($x = 1$) where the uncertain fluctuations are imposed. The same contour increment is used in all frames.*

**6.3. Standard deviations.** The dependence of the flow statistics on $\epsilon$ is briefly illustrated by analyzing the standard deviations of the scaled temperature fields. The latter are plotted in Fig. 6.6 for $\epsilon = 0.01$, 0.1, 0.2 and 0.3. As a result of this scaling, for all cases the (theoretical) value of $\sigma(\theta)$, the standard deviation of $\theta$, is 0 on the hot wall and 0.25 on the cold wall. On can observe in Fig. 6.6 that the standard deviations are not exactly equal to 0.25 on the cold wall but slightly lower. As discussed extensively in [15], this small discrepancy is due to the truncation

($N_{KL} = 4$) of the KL expansion. As observed in the Boussinesq analysis [15], the distribution of $\sigma_\theta$ exhibits a recirculation pattern that is similar to that of the mean temperature field.
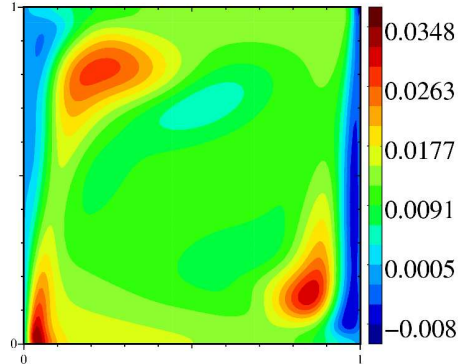


FIG. 6.7. *Le Maître et al.*

In order to obtain a better appreciation of the dependence of $\sigma_\theta$ on $\epsilon$, the difference between the standard deviation fields computed for $\epsilon = 0.01$ and $\epsilon = 0.3$ is plotted in Fig 6.7. The figure indicates that in the interior of the cavity, larger values of $\sigma_\theta$ occur for $\epsilon = 0.3$ than for $\epsilon = 0.01$. This trend does not hold along the vertical walls, where the impact of $\epsilon$ is much weaker. Also note that the differences in $\sigma_\theta$ between the solutions for $\epsilon = 0.3$ and $\epsilon = 0.01$ can be substantial, reaching approximately 14% of the imposed value along the cold wall.

**7. Conclusions.** A stochastic zero-Mach-number flow solver is developed. The solver incorporates a variable-density stochastic projection method which maintains the computational advantages of the Boussinesq solver [15]. A mass-conservative formulation is used, which is exactly implemented using a specially-tailored stochastic inverse procedure. The approach results in *decoupled* mass divergence constraints, which are inverted using a fast Poisson solver. Thus, a stable and efficient stochastic SPM for zero-Mach-number flows is constructed.

A brief validation study of the numerical scheme was first performed, based on available results for natural convection within a square cavity. The simulations were compared with available previous results from deterministic and stochastic computations. Tests under deterministic conditions included results on (a) steady-state Nusselt numbers in the Boussinesq limit and (b) steady-state thermodynamic pressure under non-Boussinesq conditions. Stochastic tests were limited to the Boussinesq regime but examined predictions of mean quantities as well as temperature and heat transfer statistics. In all cases, favorable agreement between the present predictions and previous results was obtained, thus providing support for the validity of the zero-Mach-number stochastic scheme.

The stochastic zero-Mach-number scheme was then applied to analyze the effect of the non-Boussinesq parameter $\epsilon$ on the steady-state temperature and velocity fields in a heated cavity under stochastic temperature boundary conditions. Results reveal a non-linear dependence of the mean heat transfer statistics on $\epsilon$. In particular, as $\epsilon$ increases both the Nusselt number and its standard deviation increase. The variance of the local heat flux also increases with $\epsilon$, and this effect is more pronounced along the cold wall. The mean temperature and velocity fields also depend on the Boussi-

nesq parameter, with trends resembling closely those established under deterministic conditions. On the other hand, when stochastic conditions are imposed, $\epsilon$ has a strong impact on the variance fields.

## REFERENCES

[1]  R. Cameron and W. Martin, *The orthogonal development of nonlinear functionals in series of fourier-hermite functionals*, Ann. Math., 48 (1947), pp. 385–392.

[2]  D. Chenoweth and S. Paolucci, *Natural convection in an enclosed vertical layer with large horizontal temperature differences*, J. Fluid Mech., 169 (1986), pp. 173–210.

[3]  A. Chorin, *Hermite expansions in monte-carle computation*, Journal of Computational Physics, 8 (1971), pp. 472–482.

[4]  ———, *Gaussian fields and random flow*, Journal of Fluid Mechanics, 63 (1974), pp. 21–32.

[5]  S. Crow and G. Canavan, *Relationship between a wiener-hermite expansion and an energy cascade*, Journal of Fluid Mechanics, 41 (1970), pp. 387–403.

[6]  G. De Vahl Davis and I. Jones, *Natural convection in a square cavity : a comparison exercice*, Int. Jrl. Num. Meth. in Fluids, 3 (1983), pp. 227–248.

[7]  G. De Valh Davis and I. Jones, *Natural convection in a square cavity : a comparison exercice*, Int. J. Num. Meth. Fluids, 3 (1983), pp. 227–248.

[8]  B. Debusschere, H. Najm, A. Matta, O. Knio, R. Ghanem, and O. L. Maître, *Protein labeling reactions in electrochemical microchannel flow: Numerical simulation and uncertainty propagation*, Phys. Fluids, (2002), p. submitted.

[9]  R. Ghanem, *Probabilistic characterization of transport in heterogeneous porous media*, Computer Methods in Applied Mechanics and Engineering, 158 (1998), pp. 199–229.

[10]  R. Ghanem and S. Dham, *Stochastic finite element analysis for multiphase flow in heterogeneous porous media*, Tranport in Porous Media, 32 (1998), pp. 239–262.

[11]  R. Ghanem and P. Spanos, *Stochastic Finite Elements: A Spectral Approach*, Springer Verlag, 1991.

[12]  M. Hortmann, M. Peric, and G. Scheuerer, *Finite volume multigrid prediction of laminar natural convection  : Benchmark solutions*, Int. J. Num. Meth. Fluids, 11 (1990), pp. 189–207.

[13]  O. Knio and R. Ghanem, *Polynomial chaos product and moment formulas : A user utility*, tech. report, The Johns Hopkins University, Baltimore, MD, 2001.

[14]  O. Knio, H. Najm, and P. Wyckoff, *A Semi-Implicit Numerical Scheme for Reacting Flow. II. Stiff, Operator-Split Formulation*, J. Comp. Phys., 154 (1999), pp. 428–467.

[15]  O. Le Maître, O. Knio, H. Najm, and R. Ghanem, *A stochastic projection method for fluid flow. II. Random Process*, J. Comput. Phys., 181 (2002), pp. 9–44.

[16]  O. Le Maître, M. Reagan, H. Najm, R. Ghanem, and O. Knio, *A stochastic projection method for fluid flow. I. Basic formulation*, J. Comput. Phys., 173 (2001), p. 480.

[17]  P. Le Quéré, *Accurate Solution to the Square Thermally Driven Cavity at High Rayleigh Number*, Computers Fluids, 20 (1991), pp. 29–41.

[18]  P. Le Quéré and T. de Roquefort, *Computation of natural convection in two-dimensional cavities with chebyshev polynomials*, J. Comput. Phys., 57 (1985), pp. 210–228.

[19]  P. Le Quéré, R. Masson, and P. Perrot, *A chebyshev collocation algorithm for 2d non-boussinesq convection*, J. Comput. Phys., 103 (1992), pp. 320–334.

[20]  M. Loève, *Probability Theory*, Springer, 1977.

[21]  A. Majda and J. Sethian, *The derivation and numerical solution of the equations for zero mach number combustion*, Comb. Sci. and Technology, 42 (1985), pp. 185–205.

[22]  F. Maltz and D. Hitzl, *Variance reduction in monte carlo computations using multi-dimensional hermite polynomials*, Journal of Computational Physics, 32 (1979), pp. 345–376.

[23]  W. Meecham and D. Jeng, *Use of the wiener-hermite expansion for nearly normal turbulence*, Journal of Fluid Mechanics, 32 (1968), p. 225.

[24]  H. Najm, *A Conservative Low Mach Number Projection Method for Reacting Flow Modeling*, in Transport Phenomena in Combustion, S. Chan, ed., vol. 2, Taylor and Francis, Wash. DC, 1996, pp. 921–932.

[25]  H. Najm, P. Wyckoff, and O. Knio, *A Semi-Implicit Numerical Scheme for Reacting Flow. I. Stiff Chemistry*, J. Comp. Phys., 143 (1998), pp. 381–402.

[26]  H. Paillere, C. Viozat, A. Kumbaro, and I. Toumi, *Comparison of low mach number models for natural convection problems*, Heat and Mass Transfer, 36 (2000), pp. 567–573.

[27]  S. Wiener, *The homogeneous chaos*, Amer. J. Math., 60 (1938), pp. 897–936.